#### **RESEARCH PAPER**



# Modified SAMs and templates for achieving self-alignment of full wafers

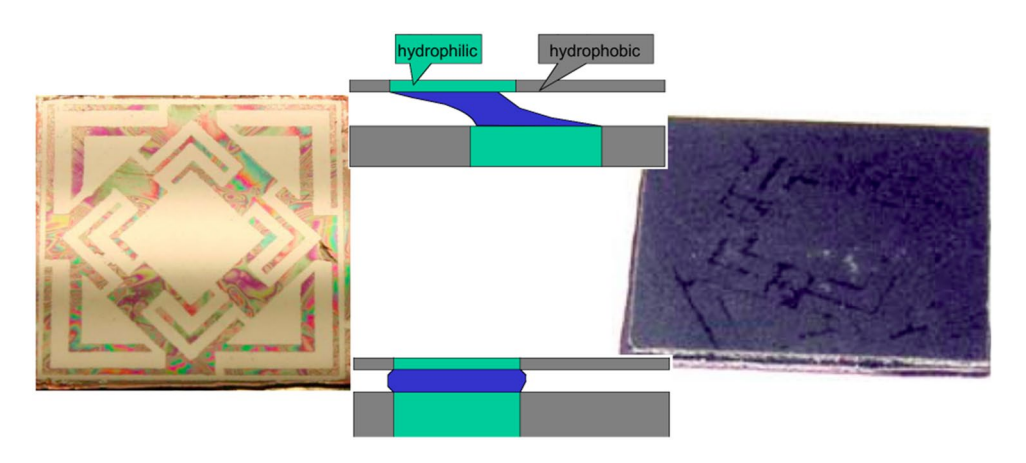
Ako Emanuel<sup>1</sup> · Ernest M. Walker III<sup>1</sup> · Hans D. Hallen<sup>1</sup>

Received: 9 February 2020 / Accepted: 17 May 2020 / Published online: 10 June 2020 © Springer-Verlag GmbH Germany, part of Springer Nature 2020

#### Abstract

Self-assembly of structures that are more than a few millimeters in size is a current problem that can have broad applications in new ways to construct the objects that we use. As a step in that direction, fluidic self-alignment at the wafer-to-wafer level is demonstrated, characterized, and modeled. Although self-alignment of millimeter-sized objects has previously been shown, several physical processes become important as the structure size is increased to a whole wafer. These processes are measured and modeled in this paper. Self-assembled monolayers, both natural and modified by oxidation, are used to create surface energy gradients that are used to produce capillary alignment forces. These forces exceed the wafer-edge forces. The measured capillary fluid profile is modeled to predict the alignment forces with no adjustable parameters. Alignment forces are measured and the trends are predicted as the surface tension of the liquid, hence the generated force, is varied. These considerations govern pattern design rules, which are described and ensure a long capture range, high alignment force, and avoidance of wafer-edge dragging.

# **Graphic abstract**



 $\textbf{Keywords} \ \ \text{Capillary force} \cdot \text{Fluid self-alignment (FSA)} \cdot \text{Hydrophobic} \cdot \text{Hydrophilic} \cdot \text{Patterned surfaces} \cdot \text{Surface chemistry}$ 

# 1 Introduction

For a long time, researchers have been aiming to create materials that will build themselves into structures. The most developed of techniques to create three-dimensional functional objects from two-dimensional parts is wafer stacking or folding (Mastrangeli et al. 2009; Mastrangeli



<sup>☐</sup> Hans D. Hallen
Hans\_Hallen@ncsu.edu

Physics Department, North Carolina State University, Raleigh, NC 27695-8202, USA

2015; Mastrangeli et al. 2011, 2017). Surface energies often dominate these self-assembling schemes when the scale of the meniscus is less than the capillary length (Böhringer 2003). A few not-self-aligning techniques such as 'Smart-View' and '3Dalign' have emerged to support wafer alignment during stacking (Lee et al. 2011). The problem is that these have been found to be costly and inaccurate when applied to tall stacks (Narimannezhad et al. 2016), and are not self-aligning. A self-aligning process would be useful in electronic packaging, where multiple wafers are difficult to view through at high resolution with IR imaging. The presence of a ground plane makes view-through impossible. The alternative, alignment from both sides, either views both sides at once with a specialized microscope or uses digital techniques to overlay the back-side image while observing the front. Both have relative positioning errors that add up. Wafer stacking has been achieved without self-alignment (Terfort et al. 1997; Ohba et al. 2010), but is limited by the interconnection requirements: 400 nm now and 200 nm for 1 μm via diameter, which enables 2 μm connection pitch (De Vos et al. 2016). Two considerations must underly the choice of self-alignment techniques. The first is the integration of bonding into the process (Sugaya et al. 2015), so that the final object is rugged. Our technique for bonding (Emanuel and Hallen 2018) uses a bonding precursor fluid in a manner that is compatible with the capillary force alignment technique described here. The second is that large temperature variations can destroy alignment, primarily due to differing thermal expansion of the wafers (Kurz et al. 2016; Gaudin et al. 2010; Lee et al. 2011). This limits the type of bonding that can be used (Dragoi et al. 2015; Flotgen et al. 2016), although low-temperature options such as ours are available (Emanuel and Hallen 2018). Our aim here is to demonstrate self-aligned stacks of wafers as an example of more general self-alignment of large (many cm-scale) structures to make a three-dimensional object. Fluidicbased self-alignment (FSA) has been done previously for few-mm-sized chips on surfaces (Xiao et al. 2016; Koyanagi et al. 2016; Fukushima et al. 2010, 2011, 2016; Terfort et al. 1997; Lu et al. 2013; Uddin et al. 2011; Fukushima et al. 2010; Gueguen et al. 2010; Sanchez et al. 2012; Arutinov et al. 2012; Chang et al. 2016, 2017; Lambert et al. 2010). Models can predict the chip process and extend to different, uniformly coated geometries (small polygons) (Böhringer et al. 2001; Chang et al. 2016; Lambert et al. 2008, 2010; Lambert and Delchambre 2005; Mastrangeli 2015; Mastrangeli et al. 2015, 2017; Tsai et al. 2007; Berthier et al. 2010, 2013), although further developments are needed as fan-out is increased (Xiao et al. 2016).

The contribution of this work is to (1) align a large, wafer level, object. The process needs to be very different from most prior work: chips have uniform surface preparation and their edges drive the alignment, even when the chips

are large (few cm) (Arutinov et al. 2015). Another study aligned wafers with arrays of uniformly sized rectangles (Martin et al. 2001); a spacer was needed, since our techniques to balance the wafer were not used. (2) The edges of the upper wafer/chip/etc. need to be rendered unimportant, so that if the patterns are slightly misplaced on the wafers, the upper wafer's position is still determined by patterns of surface treatment on the wafers, as demonstrated here. The large-scale design of the pattern, particularly the number of features, is crucial. (3) Furthermore, multiple length scales must be used, so that no local surface energy minima compete with the fully aligned state. Edges of the pattern must align both position and rotation. We check for multiple minima (Walker et al.) with a calculation similar to Böhringer et al. Böhringer et al. (2001), but must also integrate qualitative, multiple length-scales, into the pattern design. (4) Also for large wafers, excess fluid drainage must be designed by channeling in all directions, so that the wafer remains balanced and no edges drag. This advance also permits a large error in water (lubrication) volume that has previously not been tolerated, so needed to be carefully controlled by, e.g., a mist (Chang et al. 2016) or using dipping with carefully designed pads (Mastrangeli et al. 2009). (5) Prior meniscusforce modeling has involved complex modeling of specific curved structures to obtain force normal to the substrate (Chau et al. 2010; Lambert and Delchambre 2005), numerical modeling of complex droplets for flipping chips or complex alignment (Mastrangeli et al. 2011; Mastrangeli 2015; Mastrangeli et al. 2009), numerical models of forces within the plane of the surface (Brakke 1992; Chau et al. 2010; Mastrangeli 2015; Tsai et al. 2007), and simple models of linear-meniscus systems, in which the lubrication layer is either a cylinder or parallelepiped (Tsai et al. 2007; Mastrangeli et al. 2017), including dynamics (Lambert et al. 2008, 2010), although one group extended this to model the important phenomenon of meniscus unpinning (Mastrangeli et al. 2015). We do not assume a linear meniscus as the latter efforts, but instead use a Laplace-derived circular segment, and model a single, long, straight edge of a pattern at an angle from the motion of the top wafer. We verify the unstressed circular segment or stressed nearly linear meniscus with measurements, discuss the consequences of the circular meniscus, and find the results amenable to calculation of the force, edge-by-edge, on our multi-line complex patterns. (6) A prediction of the model is that the alignment force linearly approaches zero as alignment is approached. This is combatted with multiple narrow features that increase the edge length, hence increase force, to compensate. (7) Modified self-assembled monolayers (SAMs) are used to define the local surface energies to drive the capillary forces. The use of SAMs is not new, and their often long but potentially short deposition times have been discussed (Böhringer et al. 2001; Böhringer 2003; Mastrangeli et al. 2011, 2009).



What we add is a lithographic process compatible with the SAMs and a rapid process for conversion of exposed SAM from hydrophobic to hydrophilic (Hallen and Hallen 2008). We focus on the proof of concept: self-aligning on the waferscale as a starting point for the creation of functional threedimensional objects from self-assembled parts.

In this paper, a method based on surface energy minimization via capillary forces is adapted for large object selfalignment using the innovations listed above. We begin with a description of the production of self-assembled monolayers and a lithography process compatible with them. Then, we measure key features of the actual alignment process: first, a thick liquid layer cannot support a wafer, so excess liquid leaks out, while the remainder fills the hydrophilic regions of the pattern. This continues until a stable layer thickness is achieved. Due to the thin liquid layer and the relatively heavier wafer on top, the fluid layer is at a constant pressure throughout. Thus, the surface curvature is constant and the meniscus cross-section is circular, as we measure, in aligned portions. Where out of alignment, either by the initial conditions or being pushed, the meniscus cross-section becomes more linear, as we also measure. This does not support the upper wafer, of course, but the edges perpendicular to this displacement are still circular in cross-section and do so. The increased surface area of the nearly linear meniscus regions implies a larger surface energy, whose potential reduction gives the restoring, capillary force. Larger displacements can cause a breaking of this well-defined meniscus from one surface, and we observe its restoration as it heals in a propagating 'wave' along the edge. Quantification of the aligning force is achieved by modeling (with the profiles which we mentioned), and is confirmed by comparison to measurements with no adjustable parameters. Finally, we demonstrate integration with bonding and that wafer edge effects (the key alignment tool demonstrated in other papers) have been rendered unimportant compared to the alignment patterns on the wafer surface.

# 2 Experimental

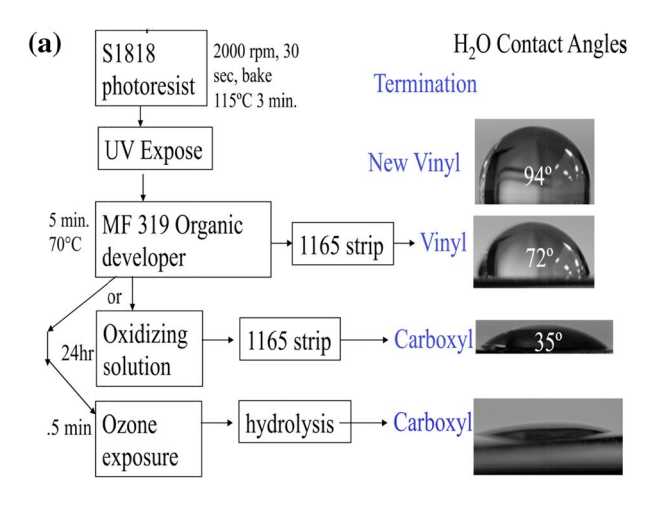
Silicon wafers with (100) orientation and varying thicknesses from 10 to 400 µm were used in these studies (Wafer World Inc. or Virginia Semiconductor). For the initial studies, thin, 1 inch-diameter wafers were aligned on thicker, 4 inch-diameter wafers. Later, data showed that the wafer thickness is not critical, but the larger scale mask design is critical, as noted above, especially if larger wafers are to be aligned. Silicon wafers were cleaned in a piranha solution of 2:1  $H_2SO_4$  (Fisher) (~ 34 N) and 30%  $H_2O_2$  for 1 h and rinsed in deionized water. The silicon surface cleaning was verified by observing wetting with water. Finally, it was spun dry at 3000 rpm and spin-rinsed with HPLC grade isopropyl

alcohol (Fisher). Wafers for self-alignment were prepared in one of two ways.

For type 1 wafers, used for the initial alignment observations only, the regions that will become hydrophilic were coated with  $\sim 30$  nm-thick aluminum in a liftoff process. Aluminum deposition was performed in diffusion-pumped high vacuum system after pumping to less than  $1 \times 10^{-6}$  torr. The entire surface was then coated with a hexadecyltrichlorosilane- (Aldrich) derived self-assembled monolayer. This was performed in a drybox with a nitrogen atmosphere, using dry hexadecane (Aldrich) as a SAM precursor solvent, and rinsing with hexadecane, dichloromethane, chloroform, then in isopropyl alcohol to remove any remainder of the precursor before removal from the drybox. The silicon wafer sample stays in one beaker throughout the whole washing, rising, and deposition. The aluminum areas are etched away with concentrated HCl (Fisher). The SAM used is particularly resistant to acid. After approximately 1 h, the areas etched free of aluminum are hydrophilic, while the areas still coated with SAM are hydrophobic.

For type 2 wafers, used for all quantitative work, the entire wafer is coated with a hydrophobic vinyl-terminated (-C=CH<sub>2</sub>) layer grown from 10-undecenyltrichlorosilane (Aldrich). The photolithography process included spincoating the samples with photoresist, baking for 3 min at 115°C, placement in the mask-aligner and exposure to UV for 7.5 s, then development in Microposit Developer 319 (Rohm&Haas), leaving the regions to be hydrophobic covered with photoresist (as above). Figure 1a shows the contact angle measurement for the surface at this point and the general process flow with contact angle measurement at several stages. Contact angles were measured via the static sessile drop method using few microliter droplet size. Images from a 5 megapixel camera with a + 10 Diopter auxiliary lens (Nikon) were analyzed by Gimp or Photoshop. Since surface energy differences drive the capillary forces, the contact angle indications of these surface energies are important. Next, the samples were rinsed in DI water and dried with nitrogen. The figure shows two oxidation schemes: a wet-chemical version that takes a long time and gives poor results, likely due to geometric constraints on the surfacebound reactant, and a fast ozonation with excellent results. Thus, we use ozonation in a UV-O<sub>3</sub> cleaner for 4 min oxidized the exposed SAM layers (Hallen and Hallen 2008). A rinse in methanol for 30 s stripped the photoresist and was followed by a rinse in DI water, to clean the samples and hydrolyze the ozone-treated areas to finish the conversion of the termination to carboxyl. Further details of the SAM-compatible photoresist processing, diagnostics of the self assembled monolayers, pattern design, and other details can be found elsewhere (Walker et al.). Figure 1b shows a patterned wafer. The presence of an SAM layer at all points of the surface permits bonding via covalent connectors





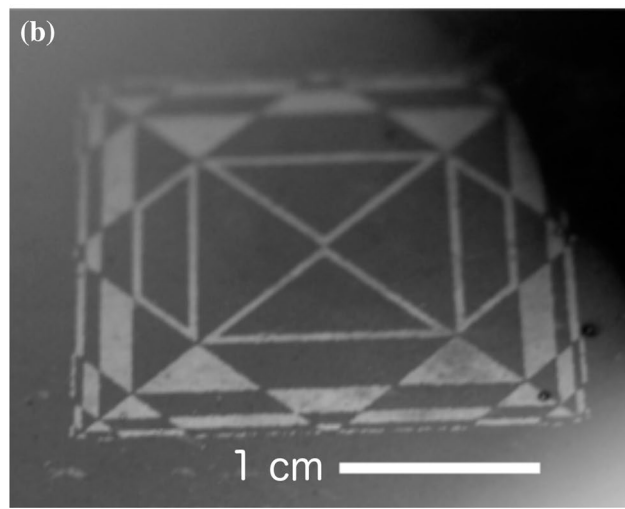


**Fig. 1** a Flowchart of the lithography process for type 2 wafers, with documentation of the effects on contact angle, **b** a wafer with a one inch square pattern photographed while under a water vapor stream to show the different water–droplet interaction with the hydrophobic (small drops form, which scatter light and are the lighter gray regions) and hydrophilic zones (smooth wetting, with only specular reflection, so appear dark at this angle)

(Emanuel and Hallen 2018) that we demonstrate at the end of the paper.

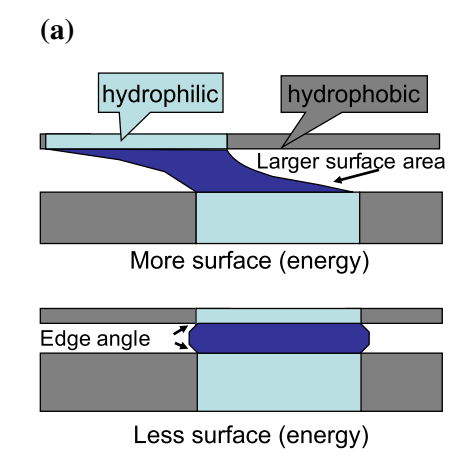
# 3 Results and discussion

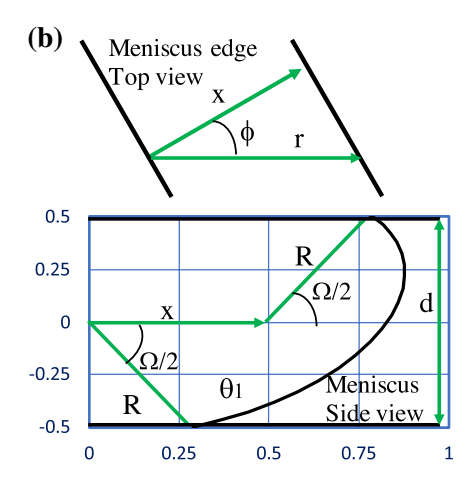
# 3.1 Capillary forces and water surface shape

First, we consider the shape of the alignment liquid surface between the wafers, the meniscus shape, and then, we will calculate the alignment force in the highly displaced and close-to-aligned regimes. When water (or other alignment, lubricant liquid) is present between the surfaces, the movement of the upper wafer is guided by the relative surface energies of the water system and the geometry of the surfaces. We can assume for a properly designed system, with adequate drainage channels and hydrophobic gaps, that the water is present only on the hydrophilic parts of the surface and that the change in the water surface area dominates the capillary force. We further ignore the corners of the pattern. This gives a simple configuration of a straight edge that when stretched by a misalignment increases the water surface area and, therefore, creates a force in the opposite direction, Fig. 2a. This single-edge-at-a-time approach will be our technique for calculation of forces on a complex pattern, one edge at a time. Since a particular edge may be at an angle to the motion, we introduce an angle  $\phi$  in the top view of Fig. 2b, the edge angles  $\theta$  in the side view and distances L, d, r and x. Our use of a sector of a circle, motivated by the Laplace curvature, rather than a straight line (Tsai et al. 2007; Mastrangeli et al. 2017, 2015) is motivated next.

It is useful to consider the forces acting on a free water droplet on a surface before adding the top wafer. The shape is driven by the pressure difference between the fluid within and the fluid outside (de Gennes et al. 2004; Martin et al. 2001):

Fig. 2 System aligns to minimize the energy of the system. a A schematic sketch, and b a top and side view diagram to illustrate the variables and geometry modeled. The side of the meniscus is a sector of angle  $\Omega$  swept, while the center moves a distance x, the offset between the wafers. The particular meniscus shown has a wafer spacing of 1 unit, a meniscus unstressed curvature radius of 0.58 units, a top wafer offset of 0.5 units, and 150° edge angles  $\theta$  on both sides







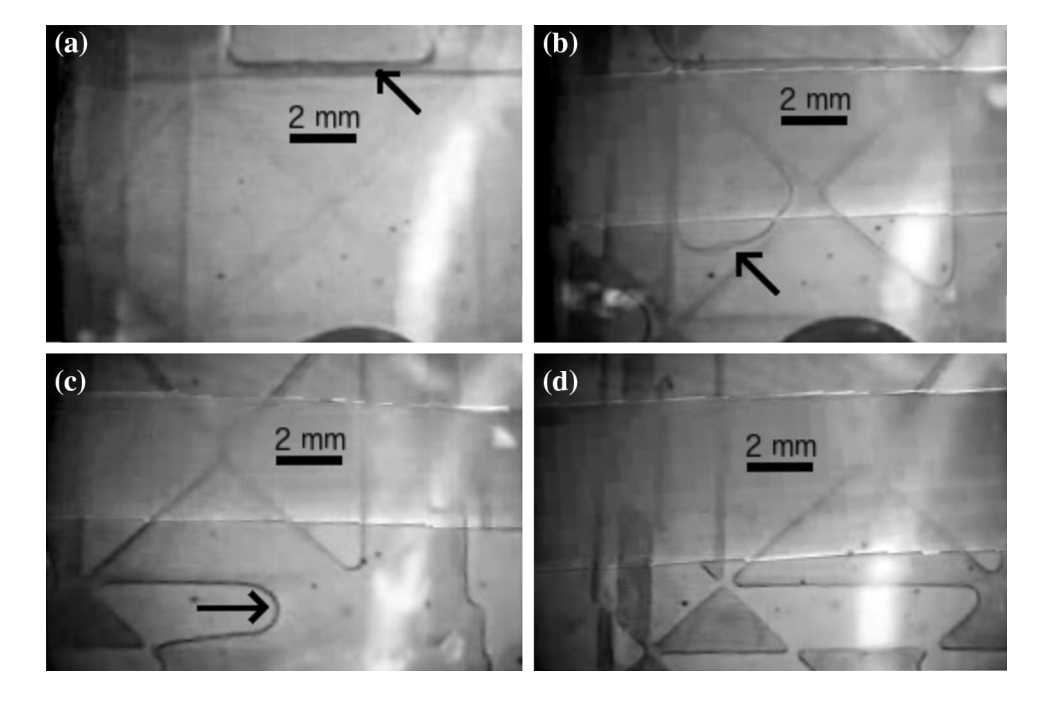
where  $\gamma$  is the surface energy of the water/air surface and the  $R_i$  are the radius of curvature of the fluid in the two perpendicular directions along the surface. In our case of a line,  $R_2$  is infinite. The pressure vs. height relation results from energy conservation,  $P_1 - P_2 = \varrho g(z_1 - z_2)$  for a fluid with density  $\rho$  and gravitation constant  $g = 9.8m/s^2$  at a height z (Halliday et al. 2013). For a free puddle, the pressure is due only to the fluid on top, so the radius of curvature increases as the top of the puddle is approached, reaching infinite at the flat top. The angle at the base is determined by the contact angle of the water on the surface. The puddle height, h, can be determined for a surface with contact angle  $\theta$  to be  $h = \sqrt{2\gamma(1-\cos\theta)/g\rho}$ . When a wafer is placed on top of the puddle, further constraints are obtained. In particular, the top surface also has an edge angle restraint, and the pressure must include the weight of the top wafer. The edge angle at the top and bottom surfaces is constrained to be in the canthotaxis sector (Mastrangeli 2015; Mastrangeli et al. 2015), but the edge formation process, by the draining of excess fluid from the hydrophobic regions, tends to make the edge angle close to the advancing contact angle of the hydrophobic surface, as we measure below. We expect it to remain there in the absence of strong perturbations to the upper wafer position. In practice, the thickness of the layer of liquid, d, between the two wafers is found to be much less than the free puddle height h, so the pressure can be considered constant throughout the liquid volume, and Eq. 1 becomes, for a wafer of mass  $m_{\text{wafer}}$  with a fluid area of  $A_{\text{contact}}$ :  $\Delta P = \text{constant} = m_{\text{wafer}} g / A_{\text{contact}} = \gamma / R$ . The constant radius due to the (almost) constant pressure everywhere within the fluid means that the water surface for the aligned case is simply a sector of a circle with constrained radius R, and top and bottom edge angles. Thus, the distance between the wafers is also constrained, at least to the degree that the edge angles remain constant. This will have important implications for design of masks for whole wafer alignment.

The arc of circle between the wafers when the edge angles in radians are  $\theta_1$  and  $\theta_2$  is  $\theta_1 + \theta_2 - \pi$ , and the length of the chord of the circle with radius R is the distance between the wafers:

$$d = 2R\sin[(\theta_1 + \theta_2 - \pi)/2]. \tag{2}$$

This thickness must be attained before a stable liquid system exists, and is evident in the progression of images as the water takes on the surface energy pattern in Fig. 3. Initially, there is excess water that the wafer floats on. Since the outer edges of the water cannot support the pressure, Eq. 1, it flows out at the sides of the wafer. This must be done uniformly, so that the wafer sides do not drag, or alignment of a whole wafer will not be attained. As the water level decreases, it begins to be driven from the hydrophobic regions, and the pattern of the alignment hydrophilic regions is impressed on the water. Arrows in Fig. 3 indicate where water edges are moving at the times given in the figure caption. As the pattern aligns, the water surface area is minimized and a stable, aligned state is reached. The wafers used in Fig. 3 are type 1 wafers and these wafers were designed with small flow (drainage) channels, so that the steps of alignment would be visible. This is why, the times are many seconds. If, as we use in our type 2 samples below, the channels are much larger, then the process

Fig. 3 a Initial placement of the upper wafer w/ offset of 600 μm, with the air bubble at top. The suction cup wafer holder is just visible at the bottom. b At 0.8 s, the sample is aligned, and air bubbles are expanding into hydrophobic zones. c After 7.1 s, air bubbles continue expanding into smaller spaces at bottom of image. d After 27 s, air bubble completely expanded into smaller spaces. This is the configuration for the displacement test





happens much more quickly (sub-second). The rate must be kept slow enough that the balance of the wafer is maintained, however, so driven by the designed channel flow and not mask or fabrication imperfections.

We have measured the shape of the water profile for both equilibrium and offset wafers by observing the shift in position of the water edge as the focus position is changed in a Nikon TE-2000 inverted optical microscope. Glass wafers are used, so that visible light can be used for the observations. We take a series of images offset by 5 µm from each other, starting at the bottom wafer (closer to the objective lens), and finding the location of the droplet edge relative to that at the surface. We find that the measurements can only be obtained for the first half of the inter-wafer displacement for the unshifted wafers, however, since the curving surface of the droplet edge near the center obscures the droplet edge below. This issue is not significant, however, since the symmetry of this case ensures that the shape above the center line mirrors that below the center line. Image analysis is used to identify the droplet edge and comparison to the reference point to calculate the offsets, as shown in Fig. 4. The close agreement to the expected circular-sector droplet edge shape is evident. The vertical and horizontal scales are different, so the shape does not look like the circle that it is.

The fit to the data in Fig. 4a is simply a portion of a circle with center constrained to be at the symmetric point of 32.5  $\mu$ m, the center of the vertical separation between the wafers, while the lateral position of the circle center and radius of curvature are allowed to vary for the best fit. The scaling makes the circle appear distorted. We find a radius of 90  $\mu$ m and an edge angle of 112°, which is larger than the static contact angle of the hydrophobic portion of the wafer, as expected for an advancing angle. When the upper wafer is pushed to the side, then the shape of this edge, perpendicular to the motion, is straightened until it

is almost a straight line, Fig. 4b, as expected. The shape of the edges parallel to the motion remains curved and supports the weight of the upper wafer.

We now calculate the alignment force. When the top and bottom patterns are displaced from each other by a distance x perpendicular to the edge, then the fluid experiences an additional force in the direction of movement. The edge angle constraints remain for sufficiently small displacements, we assume, so we can create a parametric equation for the meniscus as a circle that is linearly shifted by the distance x as the angle is swept at the same radius R through the same sector  $\Omega = \theta_1 + \theta_2 - \pi$  as the undisturbed case, Fig. 2b. This model has the advantage of guaranteeing the proper edge angle, and is appropriate for moderate displacements. For simplicity below, we take  $\theta_1 = \theta_2$ . A large displacement x yields a surface shape that is approximately a straight line. It is important to note that edges on the pattern perpendicular to the motion will experience this change in shape, whereas edges of the pattern parallel to the motion will have no change in liquid profile shape (and support the upper wafer). When an edge is not perpendicular to the motion r but at an angle  $\phi$  from that, then  $x = r\cos\phi$ . The force along x of a line segment of the pattern of length L will be given as Force<sub>r</sub> = -(dU/dx), with U the total surface energy of the system, i.e., by the rate of change in the surface area L \* (meniscus length)times the surface energy (tension,  $\gamma$ ). In particular, the length of the water, lubricant meniscus is given in terms of a dummy parametric variable  $\xi$  integrated in the range  $-\Omega/2$  to  $\Omega/2$  giving the shifting circle's x-coordinate  $u = R\cos\xi + x(\xi + \Omega/2)/\Omega$  and y-coordinate  $v = R\sin\xi$ . The spacing between the wafers is  $d = 2R\sin(\Omega/2)$ . The meniscus length S and, after interchanging the integral and derivative, the force  $F_x$  are then given by:

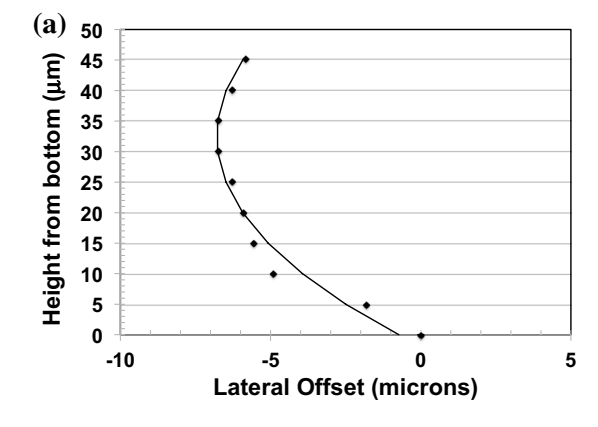
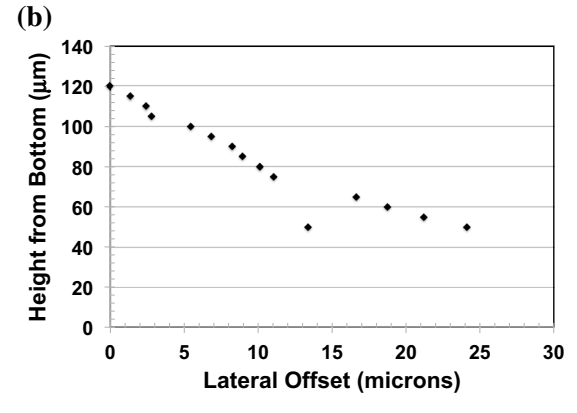


Fig. 4 Measurements of the droplet edge in a high power microscope. Focusing errors in the vertical direction are minimal and smaller than the point size. Statistical errors in the horizontal dimension are also only a few times the dot size. a The edge of the droplet in equi-



librium as a function of distance from the bottom wafer is plotted in comparison to the simple model as part of a circle (solid line). The center between the two wafers is  $32.5 \, \mu m$ . **b** Offset wafers with separation  $120 \, \mu m$  produce an edge that is approximately a straight line



$$S = \int_{-\Omega/2}^{\Omega/2} \sqrt{\left(\frac{\partial u}{\partial \xi}\right)^2 + \left(\frac{\partial v}{\partial \xi}\right)^2} d\xi$$

$$= \int_{-\Omega/2}^{\Omega/2} \sqrt{R^2 + \frac{2Rx\sin\xi}{\Omega} + \frac{x^2}{\Omega^2}} d\xi$$

$$F_x = -L\gamma (dS/dx) = L\gamma \int_{-\Omega/2}^{\Omega/2} \left(\frac{R\sin\xi}{\Omega} - \frac{x^2}{\Omega}\right) / \sqrt{R^2 + \frac{2Rx\sin\xi}{\Omega} + \frac{x^2}{\Omega^2}}.$$
(3)

For large motion,  $x = r\cos(\phi) \gg d$ , the square root term becomes equal to  $x/\Omega$ , the first term in the brackets dominates, and the constant integral cancels the remaining  $\Omega$  so the force becomes  $F_x = L\gamma$ ; that is, it becomes independent of the displacement as would be expected for a straight line. Note that if the edge is along the motion, the cosine term insures that  $x = r\cos(\phi)$  is never larger than d and the force contribution remains zero. It is interesting that when x is large enough, the orientation of the surface does not matter; it is a constant force spring. We use this simple dependence to estimate alignment forces for line segments and their orientations at the wafer level later in this paper. For small x compared to d, the square root approximates to  $R[1 - (x/R)(\sin \xi/\Omega)]$ , and its derivative in the force integral to  $[\sin \xi/\Omega - (x/R)(\cos^2 \xi/\Omega^2)]$ . The first term is odd on an even integration range so integrates to zero. The second term gives the force  $F_x = L\gamma(x/R)(1 - \sin\Omega/\Omega)/(2\Omega)$ . This sharpens the response to line segments perpendicular to the motion, and has the unwanted feature of reduced force as alignment is approached. Increasing the number of lines for small offsets can ameliorate this reduction; that is, using many thin parallel lines (or small features for multiangle alignment) will ensure sufficient force even for small displacements from equilibrium, and will be present in our mask designs.

# 3.2 Self-alignment

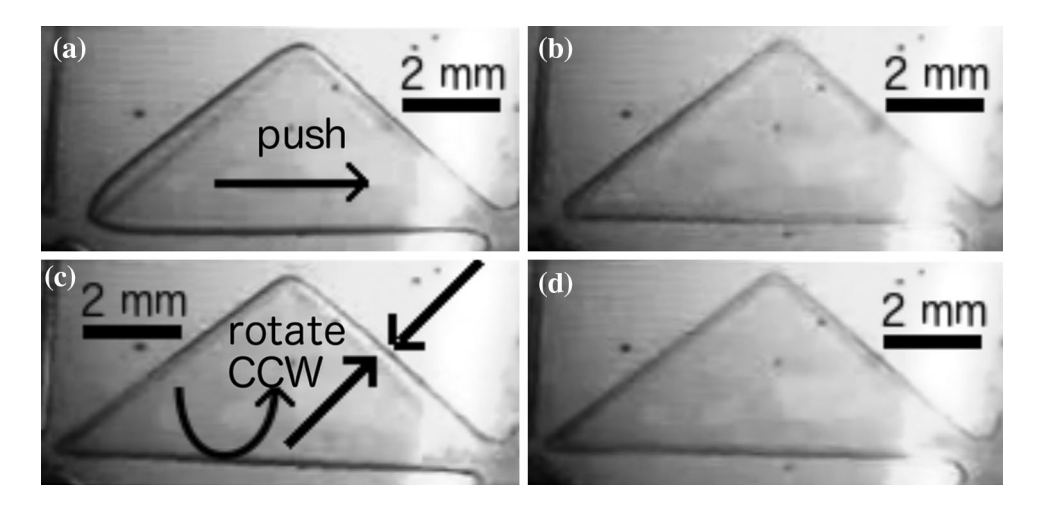
The particular pattern of hydrophilic and hydrophobic zones on a type 1 wafer was chosen to have both a large capture offset and avoid local minima that would result in mis-alignment. Thus, the patterns contain both large and small zones, and they are arranged in a non-periodic manner. Smaller zones were provided far from the wafer center, so that both angular and linear alignment would be accurate. The pattern of the zones is the same on both wafer surfaces. The smallest feature size on the mask was  $\sim 265~\mu m$ , and the (important) edge smoothness is a few microns. Once the pattern was transferred to the wafers as described above, one surface was coated by a light spray of water, and the second wafer lowered onto it with an offset of  $\sim 1{\text -}2$  mm from the aligned position. The wafers

were observed using a low-power inspection microscope fitted with a 100 W light bulb as an IR source and a small CCD camera on an eyepiece adaptor for imaging in transmission. The IR passes through the silicon wafers and is captured by the CCD camera. Air bubbles were observed to expand into the regions with hydrophobic coating (leaving water in the hydrophilic zones), filling the larger areas in less than 10 s and the smaller zones within a minute, Fig. 3. At that point, the top wafer had aligned itself to the bottom wafer to within the resolution of the microscope set-up. The fact that the observed alignment is better than the smallest mask feature size is not surprising. It should be limited by the edge accuracy, which is  $\sim$  10 times smaller, or overall mask distortion. Thus, we expect that the alignment is significantly below our observation limit.

The self-alignment capability was checked by intentionally displacing the aligned wafers using tweezers. Within a capture radius of a few mm in all directions and rotation of several degrees, the wafers re-aligned themselves to better than our observation resolution. Examples of the wafers in the displaced state and after self re-alignment are shown in Fig. 5. The microscope is in focus on the lower wafer position, so the upper wafer appears with less contrast, as indicated by the arrows in Fig. 5c. The IR images capture the displacement of the water-air boundary during displacement, and the edge contrast indicates that the water surface is indeed being stretched. When the wafers are pushed even further out of alignment (tenths of a mm, about the thickness of the water layer), this water boundary stretch is sufficient to break the water contact to the lower wafer over portions of the edge. A trial with displacement vertical in the picture resulted in a water break that is symmetric about the triangle point and re-heals again by 'waves' propagating down the edge is shown in Fig. 6a, until realignment, Fig. 6b. The top and bottom wafer pattern edges are also indicated by arrows in the figure. This type of behavior is observed often for large displacements from equilibrium, although the symmetry is not often present. A good model for de-pinning exists in the literature (Mastrangeli et al. 2015), so we do not create a new one here. The dynamics of the re-pinning are of future interest.

More accurate measurements of the alignment were made with type 2 samples and higher resolution masks. A reference point was used on the upper wafer, while it was viewed with a Nikon TE-2000 microscope at  $200 \times$  magnification. The resolution of the optical and camera system was better than 1  $\mu$ m. After the initial alignment was achieved, the wafer was deliberately pushed or rotated out of alignment by 1 mm and then allowed to return to the aligned position. The displacement of the reference point from the initial alignment point was used as an indicator of the alignment accuracy. This was repeated many times. The alignment accuracy, given by averaging several trials, was 3–5  $\mu$ m.

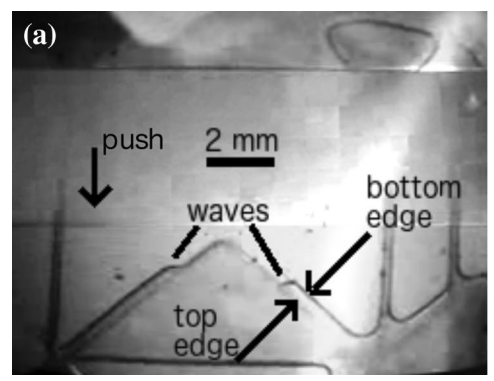


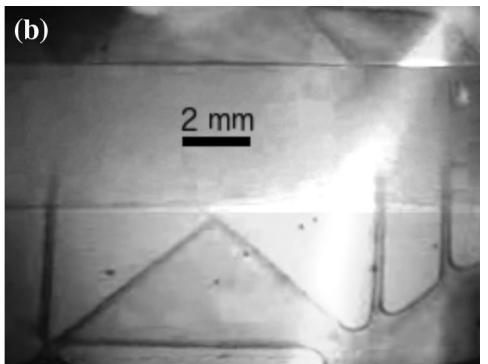


**Fig. 5** IR imaging of successful alignment of two stacked Si wafers to better than the imaging resolution of  $60 \mu m$ . The top wafer was displaced laterally (a) and allowed to relax to the aligned state (b), then rotationally displaced (c) and released to return to center (d).

Examples are shown in the figure for a few millimeter offsets. The base of the triangle is 8.5 mm, and the region inside the triangle has a hydrophilic coating and is darkened by the water present between the wafers, while the surrounding, hydrophobic, regions lack water

Fig. 6 IR imaging of successful realignment of the top wafer in a two Si wafer stack. The displacement is sufficient to partially break the connection of water to the bottom wafer, which reconnects during self-realignment as a 'wave' moving along the edge, as seen in a. The realignment is complete in b





While this level is adequate, more care to mask quality and distortion reduction would improve the alignment quality.

### 3.3 Measurements of the alignment force

The alignment model can be tested by measurement of the alignment force in a realistic system. We use the pattern on the sample shown in Fig. 7 and type 2 wafers. This pattern contains enough hydrophilic zones to retain sufficient water (lubricant, bonding fluid) to suspend the top wafer. Also, the hydrophilic regions are connected to provide flow of fluid throughout the design. This will level the overall fluid levels and keep the top wafer flat. Otherwise, the wafer may contact at some point and cause too much friction. Finally, the design has drainage flow channels for allowing the fluid level to slowly lower as the top wafer lines up with the bottom features. The design of the pattern has clear flow paths to insure that no water bridging across hydrophobic areas will be left as alignment occurs. The top and bottom wafers fabricated with mirror-image patterns derived (ozone oxidized

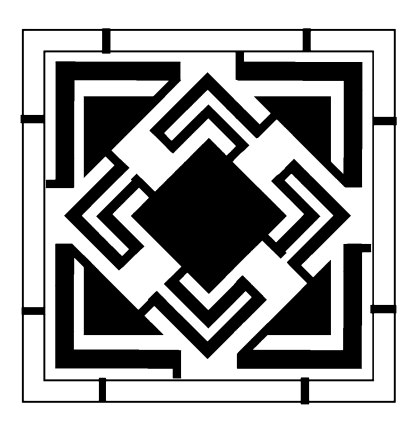


Fig. 7 The pattern used for alignment force measurements. The overall (outer square) dimension is 1 inch

to create hydrophilic regions with the pattern) solely from 10-UTS (hexadecenyltrichlorosilane) SAMs, which have a vinyl, -C=CH<sub>2</sub> termination. The pattern showed a strong alignment tendency for a few seconds, then, as intended,



the liquid escaped through flow channels until the top wafer came to rest on the bottom wafer. If dried and rewetted (with a small drop of DI water in the center 0.05 mL), the selfalignment resumes again. Thus, the alignment force studies need to be completed, while the wafer is floating, so the wafer had to be initially positioned to within a few mm of the aligned position. This was accomplished reproducibly with the use of suction tweezers.

The calculation of the force follows from the force relations for a straight line segment derived above. The pattern is shown in Fig. 7 and the lengths of the segments shown in Table 1. Figure 7 shows the hydrophilic areas as black, and these are the regions in the table, going from the center

Table 1 Lengths of the segments of the dark region edges in the pattern are quantified

Edge	$\Delta x$	Δy	Edge	$\Delta x$	Δy
Center	6063	6063	Hypotenuse	5601	5601
1st br f	1326	1326	8th br f	1529	1529
1st br b	419	419	8th br b	1100	1100
2nd br f	3228	3228	Triangle s 1	5832	0
2nd br b	2113	2113	Triangle s 2	0	5832
3rd br f	2809	2809	9th br end	1069	0
3rd br b	2476	2476	9th br f	0	8204
4th br f	1847	1847	9th br b	0	8875
4th br b	485	485	10th br f	6990	0
5th br f	4402	4402	10th br b	9649	0
5th br b	3228	3228	10th br end	0	2151
6th br f	3863	3863	Stub to 10th b	0	732
6th br b	3675	3675	Periphery	25047	0
7th br f	1499	1499	Periphery b	25664	0
7th br b	980	980			

in µm. Branch numbering starts at the center and proceeds to the outside; there are four copies of each

br branch, f front, b back, and s side. Both  $\Delta x$  and  $\Delta y$  are measured (a) 0.15 0.1 plateau Force (N) 0.05 • 0% **10%** 

20%

o 30%

5

Fig. 8 a The force as a function of displacement of the top wafer is compared for several fluids with different surface tensions, created by different dilutions of ethanol in water (percent by volume noted). **b** 

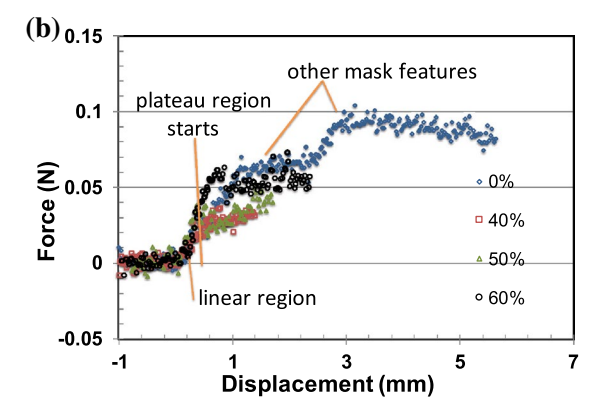
3

Displacement (mm)

-0.05

outwards. One of the four dark paths is followed, with each segment labeled as a branch except the triangle and the periphery. The lengths of each segment are calculated. There are four of each segment, each side counts separately. The edges are either at  $\phi = 0$ , 45 or 90°, so all but those at 90° will contribute  $F_{\nu} = L\gamma$  as found above. Not shown in the table is the second periphery, which is about twice the tenth branch end longer than the inner periphery. Adding these all together gives a weighted length of 0.582 m for the pattern.

To test the force calculation ability for more than one case with a single pattern, we use fluids with different surface tensions. This is achieved by mixing water with increasing concentrations of ethanol, which reduces the surface tension. The surface tensions can be obtained from the literature or measured from contact angles on the same surface. We find for concentrations of ethanol of 0, 10, 20, 30, 40, 50, and 60% surface tensions of 73.1, 67.5, 58.5, 53.8, 50.6, 48.7, and 47.4 mN/m from contact angle measurements (Emanuel 2011). The alignment force measured as a function of top wafer displacement and fluid is shown in Fig. 8. The smaller dilutions are shown in (a), and the larger with pure water repeated as a reference in (b). The forces were measured on a constant speed linear motion stage equipped with a cantilever force sensor (Futek) that pushed on the upper wafer. The abscissas have been corrected for the (very small) effects of sensor bending. The qualitative features are as expected: it starts linearly as we predicted for small displacements, and saturates to a constant value as predicted for large displacements. The data at different ethanol concentrations saturate at the near the same offset, 0.3–0.5 mm, and less than the distance between pattern features, as expected, since this should be approximately where the offset equals the fluid thickness. This argument apparently fails when the surface tension is very large and the displacement needed to reach the linear regime is longer, 0.7 mm. Some of the data in the figure contain several linear rises followed by plateaus



As a, but higher ethanol concentrations, and with pure water repeated as a reference



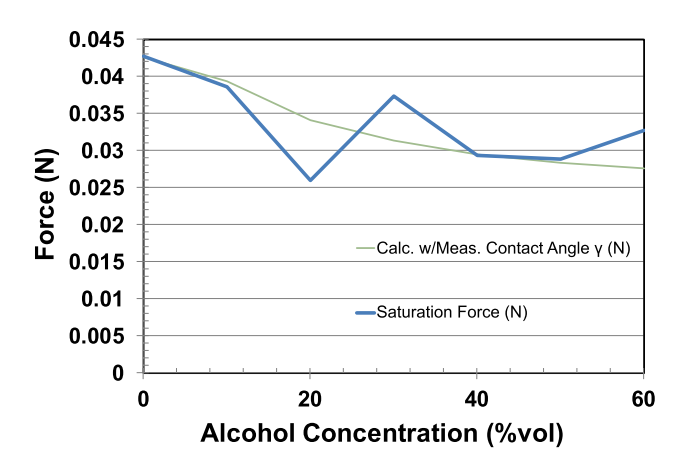


Fig. 9 The measured saturation alignment force is compared to calculations with no adjustable parameters

and other complications. Comparing the offsets where these other features are found in Fig. 8 with the pattern structure shown in Fig. 7, one finds that line segments in the pattern can correlate to more than just the matching segment of the other pattern, but also to a neighboring segment. Some 'extra' features relate to such occurrences. Other features relate to experimental problems such as dust on the surfaces.

The measured force, which is taken as the saturation value close to where all the fluids saturate, is compared in Fig. 9 to the theoretical calculation based on the surface tensions and edge lengths described above. There are no adjustable parameters. The trends of the data are reproduced well, although there remain fluctuations about the calculation, likely due to errors in locating the precise saturation point. This error is minimized by ensuring reasonable values for the saturation distance (close to the fluid thickness), and is probably about 10%. The proximity of neighboring pattern features close to this displacement also contributes to the uncertainty.

The speed of the alignment process depends upon the amount of excess alignment fluid and the drainage channel size as discussed above, and also on the forces and viscosity of the alignment fluid itself. A lower viscosity increases the channel flow rate to speed that part of the process, but also reduces the alignment force, as we have just observed. This can be overcome by more edges acting at once, which allowed the entire process on our fast-draining mask design of Fig. 7 to take place in less than a second. Inertia can also help speed the final alignment process (Arutinov et al. 2015; Lambert et al. 2010).

# 3.4 Integration

These all-SAM surfaces can be incorporated into a covalent nanoglue (Emanuel 2011; Emanuel and Hallen 2018), that will allow bonding once alignment is achieved. The

nanoglue creates a chain of covalent bonds between two surfaces. It begins with SAM bonds to each surface: one is a hydroxyl bond as we use here and another is an amine bond that is also hydrophilic and we have used for alignment. Using an alignment liquid that contains a partially aligned nylon precursor with the pattern in Fig. 7, a moderate temperature rise of ~ 100–200°C forms the peptide bonds between the aligned surfaces. The nylon 6–6 bonding solution showed an even stronger alignment tendency than plain DI water alone, and the alignment pattern could be seen more clearly with nylon 6,6 solution. Use of the nylon solution, however, destroyed the pattern, as diamine molecules bonded with the exposed carboxylic acid functional groups. This is a natural part of the bonding process, but does not allow realignment tests. The final bond, Fig. 10, is stronger than the wafer, meaning that the wafer breaks and the bond cannot be pried apart, extending the idea to the realm of practicality. One concern noted above about the alignment of two patters when the patterns are shifted relative to the wafers. If the edge of the wafer contributes a large fraction of the force, the edges of the wafer may dominate the alignment, as in prior chip alignments. We used a large pattern-edge length in the pattern to overcome the wafer edges, and indeed, the edges of the wafer do not align, as observed in Fig. 10, while the pattern does.

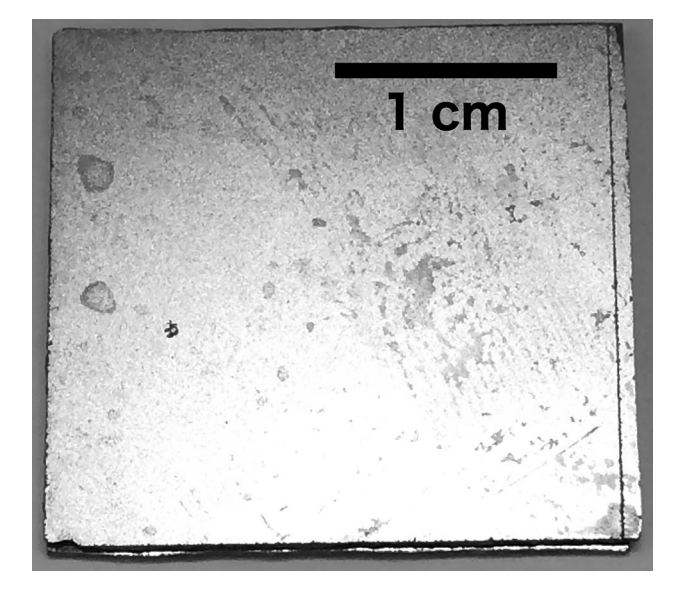


**Fig. 10** A pair of patterned wafers approximately 1 inch square were aligned with a covalent nanoglue used as both an alignment fluid and bonding agent. These wafers are bonded together with pattern (but not external edge) alignment. Photoresist still on the 'flip' side can be seen on the bonded pair



#### 4 Conclusions

Self-alignment can be made to occur at the full-wafer-level to an accuracy approaching that required for realistic wafer stacking by using a hydrophilic/hydrophobic pattern made from a single SAM layer with patterned oxidation. Capillary forces drive the alignment, with pattern features at several length scales to eliminate local minima, many narrow pattern features to ensure adequate force near alignment, and provision of drainage channels to balance the aligning wafer as fluid escapes prior to bonding. A simple model for the meniscus and the alignment force which it provides is used to calculate the alignment force on a patterned wafer set, which compares favorably to measurements. Demonstration of integration with a bonding fluid demonstrates that the pattern, not upper wafer edges, dominates the alignment, as desired.

**Acknowledgements** This work was supported by AFRL-WPAFB (Grant FA8650-04-2-1619).

#### References

- Arutinov G, Smits ECP, Mastrangeli M, Heck G, Brand J, Schoo HFM, Dietzel A (2012) Capillary self-alignment of mesoscopic foil components for sensor-systems-in-foil. J Micromech Microeng 22:115022
- Arutinov G, Mastrangeli M, Smits ECP, van Heck G, den Toonder JMJ, Dietzel A (2015) Foil-to-foil system integration through capillary self-alignment directed by laser patterning. J Microelectromech Syst 24:126–133
- Berthier J, Mermoz S, Brakke K, Sanchez L, Fretigny C, Cioccio LD (2013) Capillary self-alignment of polygonal chips: A generalization for the shift-restoring force. Microfluid Nanofluid 14:845–858
- Berthier J, Brakke K, Grossi F, Sanchez L, Di Cioccio L (2010) Selfalignment of silicon chips on wafers: a capillary approach. J Appl Phys 108
- Böhringer KF (2003) Surface modification and modulation in microstructures: controlling protein adsorption, monolayer desorption and micro-self-assembly. J Micromech Microeng 13:S1–S10
- Böhringer K, Srinivasan U, Howe R (2001) Modeling of capillary forces and binding sites for fluidic self-assembly. Technical Digest. MEMS 2001. 14th IEEE International Conference on Micro Electro Mechanical Systems (Cat. No.01CH37090). pp 369–374, ISSN: 1084-6999
- Brakke KA (1992) The surface evolver. Exp Math 1:141–165. https://doi.org/10.1080/10586458.1992.10504253
- Chang B, Zhou Q, Wu Z, Liu Z, Ras RHA, Hjort K (2016) Capillary self-alignment of microchips on soft substrates. Micromachines 7:41
- Chang B, Zhu Z, Koverola M, Zhou Q (2017) Laser-assisted mist capillary self-alignment. Micromachines 8:361
- Chau A, Régnier S, Delchambre A, Lambert P (2010) Theoretical and experimental study of the influence of AFM tip geometry and orientation on capillary force. J Adhes Sci Technol 24:2499–2510
- de Gennes P-G, Brochard-Wyart F, Quéré D (2004) Capillarity and wetting phenomena. Springer, New York
- De Vos J, Peng L, Phommahaxay A, Van Ongeval J, Miller A, Beyne E, Kurz F, Wagenleiter T, Wimplinger M, Uhrmann T (2016)

- Importance, of alignment control during permanent bonding and its impact on via-last alignment for high density 3D interconnects. In: IEEE International 3D Systems Integration Conference (3DIC). Piscataway, NJ, USA 2016:5
- Dragoi V, Burggraf J, Kurz F, Rebhan B (2015) 3D integration by wafer-level aligned wafer bonding. In: Proceedings of the international semiconductor conference, CAS. Sinaia, Romania, pp 185–188
- Emanuel A (2011) A novel covalent nanoglue and whole wafer selfalignment based upon self-assembled monolayers. Ph.D. Dissertation, North Carolina State University, Raleigh
- Emanuel A, Hallen HD (2018) A self-assembled covalent nanoglue. Transl Mater Res 5:025001
- Flotgen C, Razek N, Dragoi V, Wimplinger M (2016) Conductive semiconductor interfaces fabricated by room temperature covalent wafer bonding. ECS Transactions, Honolulu, pp 45–51
- Fukushima T, Hashiguchi H, Kino H, Tanaka T, Murugesan M, Bea J, Hashimoto H, Lee K, Koyanagi M (2016) Transfer and non-transfer 3d stacking technologies based on multichip-to-wafer self-assembly and direct bonding. In: Proceedings—electronic components and technology conference. Las Vegas, NV, United States, pp 289–294
- Fukushima T, Iwata E, Konno T, Bea J-C, Lee K-W, Tanaka T, Koyanagi M (2010) Surface tension-driven chip self-assembly with load-free hydrogen fluoride-assisted direct bonding at room temperature for three-dimensional integrated circuits. Appl Phys Lett 96
- Fukushima T, Iwata E, Lee K.-W, Tanaka T, Koyanagi M (2010) Self-assembly technology for reconfigured wafer-to-wafer 3D integration. In: Proceedings—electronic components and technology conference. Las Vegas, NV, United states. pp 1050–1055
- Fukushima T, Iwata E, Ohara Y, Murugesan M, Bea J, Lee K, Tanaka T, Koyanagi M (2011) Multichip self-assembly technology for advanced die-to-wafer 3-D integration to precisely align known good dies in batch processing. In: IEEE transactions on components, packaging and manufacturing technology. 445 Hoes Lane / P.O. Box 1331, Piscataway, NJ 08855-1331, United States; pp 1873–1884
- Gaudin G, Riou G, Landru D, Tempesta C, Radu I, Sadaka M, Winstel K, Kinser E, Hannon R (2010) Low temperature direct wafer to wafer bonding for 3D integration: Direct bonding, surface preparation, wafer-to-wafer alignment. In: IEEE 3D system integration conference, (2010) 3DIC 2010. Munich, Germany, p 2010
- Gueguen P, Ventosa C, Cioccio LD, Moriceau H, Grossi F, Rivoire M, Leduc P, Clavelier L (2010) Physics of direct bonding: Applications to 3D heterogeneous or monolithic integration. Microelectron Eng 87:477–484
- Hallen MA, Hallen HD (2008) Synthesis of carboxylic acid monolayers by ozonolysis of 10-undecenyltrichlorosilane SAMs. J Phys Chem C 112:2086–2090
- Halliday D, Resnick R, Walker J (2013) Fundamentals of physics, 10th edn. Wiley, Oxford
- Koyanagi M, Lee K, Fukushima T, Tanaka T (2016) New multichipto-wafer 3D integration technology using Self-Assembly and Cu nano-pillar hybrid bonding. In: 2016 13th IEEE international conference on solid-state and integrated circuit technology, ICSICT 2016—proceedings. Hangzhou, China, pp 338–341
- Kurz F, Plach T, Suss J, Wagenleitner T, Zinner D, Rebhan B, Dragoi V (2016) High precision low temperature direct wafer bonding technology for wafer-level 3D ICs manufacturing. ECS Trans (USA) 75:345–53
- Lambert P, Delchambre A (2005) Parameters ruling capillary forces at the submillimetric scale. Langmuir 21:9537–9543
- Lambert P, Chau A, Delchambre A, Régnier S (2008) Comparison between two capillary forces models. Langmuir 24:3157–3163



- Lambert P, Mastrangeli M, Valsamis J-B, Degrez G (2010) Spectral analysis and experimental study of lateral capillary dynamics for flip-chip applications. Microfluid Nanofluid 9:797–807
- Lee SH, Chen K-N, Lu JJ-Q (2011) Wafer-to-wafer alignment for three-dimensional integration: A review. J Microelectromech Syst 20:885–898
- Lu J, Nakano Y, Takagi H, Maeda R (2013) High-efficient chip to wafer self-alignment and bonding applicable to MEMS-IC flexible integration. IEEE Sens J 13:651–656
- Lu J, Takagi H, Nakano Y, Maeda R (2013) Size-free MEMS-IC highefficient integration by using carrier wafer with self-assembled monolayer (SAM) fine pattern. In: Proceedings—electronic components and technology conference. Las Vegas, NV, United states, pp 1508–1513
- Martin BR, Furnange DC, Jackson TN, Mallouk TE, Mayer TS (2001) Self-alignment of patterned wafers using capillary forces at a water-air interface. Adv Funct Mater 11:381–386
- Mastrangeli M (2015) The fluid joint: the soft spot of micro- and nanosystems. Adv Mater 27:4254–4272
- Mastrangeli M, Abbasi S, Varel C, Hoof CV, Celis J-P, Böhringer KF (2009) Self-assembly from milli- to nanoscales: methods and applications. J Micromech Microeng 19:083001
- Mastrangeli M, Ruythooren W, Hoof CV, Celis J-P (2009) Conformal, dip-coating of patterned surfaces for capillary die-to-substrate self-assembly. J Micromech Microeng 19:045015
- Mastrangeli M, Ruythooren W, Celis J-P, Van Hoof C (2011) Challenges for capillary self-assembly of microsystems. IEEE Trans Compon Packag Manuf Technol 1:133–149
- Mastrangeli M, Arutinov G, Smits ECP, Lambert P (2015) Modeling capillary forces for large displacements. Microfluid Nanofluid 18:695–708
- Mastrangeli M, Zhou Q, Sariola V, Lambert P (2017) Surface tensiondriven self-alignment. Soft Matter 13:304–327
- Narimannezhad A, Jennings J, Weber M, Lynn K (2016) Pushing the limits of bonded multi-wafer stack heights while maintaining high precision alignment. J Microelectromech Syst (USA) 25:725–36

- Ohba T, Maeda N, Kitada H, Fujimoto K, Suzuki K, Nakamura T, Kawai A, Arai K (2010) Thinned wafer multi-stack 3DI technology. Microelectron Eng 87:485–490
- Sanchez L, Bally L, Montmayeul B, Fournel F, Dafonseca J, Augendre E, Di Cioccio L, Carron V, Signamarcheix T, Taibi R, Mermoz S, Lecarpentier G (2012) Chip to wafer direct bonding technologies for high density 3D integration. In: Proceedings–electronic components and technology conference. San Diego, CA, United states, pp 1960–1964
- Sugaya I, Mitsuishi H, Maeda H, Tsuto T, Nakahira H, Okada M, Okamoto K (2015) Precision wafer bonding process for future cost-effective 3DICs. In: 26th Annual SEMI advanced semiconductor manufacturing conference, ASMC. Saratoga Springs, NY, United states, 2015, pp 429–434
- Terfort A, Bowden N, Whitesides GM (1997) Three-dimensional selfassembly of millimetre-scale components. Nature 386:162–164
- Tsai CG, Hsieh CM, Yeh JA (2007) Self-alignment of microchips using surface tension and solid edge. Sens Actuators A Phys 1–2:343–349
- Uddin A, Milaninia K, Chen C.-H, Theogarajan L (2011) Wafer scale integration of CMOS chips for biomedical applications via selfaligned masking. In: IEEE transactions on components, packaging and manufacturing technology. 445 Hoes Lane / P.O. Box 1331, Piscataway, NJ 08855-1331, United States. pp 1996–2004
- Walker III EM, Emanuel A, Hallen HD. Self alignment of whole wafers using patterning for capillary forces (submitted)
- Xiao J, Chaudhuri RR, Seo S-W (2016) Heterogeneous Integration of Thin-Film Optical Devices Utilizing Fluidic Self-Assembly and Micro-Pick-and-Place Technique. IEEE Trans Compon Packag Manuf Technol 6:1283–1289

**Publisher's Note** Springer Nature remains neutral with regard to jurisdictional claims in published maps and institutional affiliations.

